Acta Crystallographica Section A
Foundations of Crystallography
ISSN 0108-7673

Received 7 March 2011
Accepted 30 March 2011

The development of Laue techniques for single-pulse diffraction of chemical complexes: time-resolved Laue diffraction on a binuclear rhodium metal-organic complex

Anna Makal, Elzbieta Trzop, Jesse Sokolow, Jaroslaw Kalinowski, Jason Benedict and Philip Coppens*

Chemistry Department, University at Buffalo, State University of New York, Buffalo, NY 14260-3000, USA. Correspondence e-mail: coppens@buffalo.edu

A modified Laue method is shown to produce excited-state structures at atomic resolution of a quality competitive with those from monochromatic experiments. The much faster data collection allows the use of only one or a few X-ray pulses per data frame, which minimizes crystal damage caused by laser exposure of the samples and optimizes the attainable time resolution. The method has been applied to crystals of the α-modification of $Rh_2(\mu\text{-PNP})_2(PNP)_2\,(BPh_4)_2$ [PNP = $CH_3N(P(OCH_3)_2)_2$, Ph = phenyl]. The experimental results show a shortening of the Rh—Rh distance in the organometallic complex of 0.136 (8) Å on excitation and are quantitatively supported by quantum-mechanical (QM)/molecular-mechanics (MM) theoretical calculations which take into account the confining effect of the crystal environment, but not by theoretical results on the isolated complex, demonstrating the defining effect of the crystal matrix.

1. Introduction

Time-resolved (TR) X-ray crystallography at advanced light sources is a frontier area bound to undergo dramatic new developments with the advent of ultrabright X-ray free-electron lasers (XFELs). Earlier TR studies of chemical systems in which atomic resolution was reached have used monochromatic radiation for which methods are well developed and a reasonable accuracy can be achieved (Coppens, Benedict *et al.*, 2010; Cailleau *et al.*, 2010). The use of monochromatic data avoids the wavelength dependence of both the scattering process and the detector response and does not suffer from the broadening of the reflection maxima inherent in the Laue technique. However, with a narrow bandwidth of monochromatic radiation only a very small fraction of the photons in the synchrotron beam are productively used, even at undulator-equipped beamlines. Thus a longer exposure time and therefore more pulses are required, which limits the time resolution that can be achieved. Furthermore, the longer exposure time implies more extensive laser exposure, thereby enhancing the temperature increase of the sample due to light absorption.

It follows that for picosecond-timescale TR diffraction at synchrotron sources the use of polychromatic radiation is imperative. To achieve this goal we have developed a number of methods to improve the accuracy and interpretation of Laue measurements. They include the RATIO technique in which the measured I_{ON}/I_{OFF} ratios are used in combination with a set of monochromatic data collected at the same temperature (Coppens *et al.*, 2009), photo-Wilson plots to estimate the temperature increase due to the laser exposure of the sample (Schmøkel *et al.*, 2010), the definition of R factors specific for dynamic structure crystallography (Coppens, Kamiński & Schmøkel, 2010), and a scaling technique for relative scaling within multi-crystal data sets collected on the same substance. The scaling is required for calculation of the photodifference maps using all available reflections. The technique is based on the moduli of the absolute fractional intensity change and is described in §2.3. We describe a single-pulse Laue diffraction experiment of a binuclear Rh^I complex in which the techniques summarized above have been applied and a comparison of the results with theoretical calculations. A preliminary account of the results of this study has been published (Benedict *et al.*, 2011).

2. The experiment

2.1. Crystal structure and photochemical properties

The crystal structures of the three polymorphs of $Rh_2(\mu\text{-PNP})_2(PNP)_2(BPh_4)_2$, (1), where PNP = $CH_3N(P(OCH_3)_2)_2$ and Ph = phenyl (Fig. 1), and related salts were reported by Mague and coworkers (Blakley *et al.*, 1989; Mague, 1995). On excitation of the α form with 337 nm light at 10 K a strong emission band was observed at 730 nm, but at $\sim$ 50 K a second band develops at 780 nm, while the band at 730 nm weakens and disappears at 80 K. The change is attributed to a thermal transition to a second triplet state of somewhat lower energy,

Table 1
Cell dimensions and emission properties.

Compound	Space group	Cell dimensions (Å) 225 K, $Z = 4$	Excitation wavelength (nm)	Lifetime (µs) (Blakley *et al.*, 1989)	Emission wavelength† (nm) (Blakley *et al.*, 1989)
$[Rh_2PNP_4][BPh_4]_2$ α modification	$P2_1/n$	a = 13.9783 (3) b = 20.2046 (5) c = 28.1465 (7) β = 90.8420 (10)	337	35.3 (10 K) 46.5 (10 K)	718 (10 K) 790 (10 K)

† Wavelength at which the emission was monitored.

separated from the higher state by an activation barrier (Blakley *et al.*, 1989). The large Stokes shift observed indicates a significant structural rearrangement on excitation. Owing to a broadening of the spot shape in the Laue patterns on cooling attributed to strain induced in the specimen crystals, the current experiment was performed at 225 K by cooling in a nitrogen stream. Unit-cell information from the monochromatic experiment and luminescence properties are summarized in Table 1. Full crystallographic information on the ground-state structure is given in the supplementary material.[1] The 225 K temperature of the experiment reported here implies that the excited state with the 780 nm emission was studied. The resulting shortening of the emission lifetime from the value of 46.5 (3) µs reported at 10 K (Blakley *et al.*, 1989) does not affect the current experiment as the delay between the 35 ps pump and 100 ps probe pulses was only 100 ps.

2.2. Data collection

Time-resolved intensity data were collected at the 14-ID BioCARS station at the Advanced Photon Source. Two different undulator settings were used with peak energies at 12 and 15 keV, respectively. The corresponding spectral distributions are illustrated in Fig. 2. Use of the polychromatic beam ($\Delta E/E = \sim 8\%$) allows collection of a frame of data with a single 100 ps synchrotron pulse (Fig. 3). The samples were pumped with 35 ps pulses of a Ti:sapphire laser tuned to a wavelength of 390 nm. The laser power varied between 0.45 and 0.6 mJ mm^{-2}. It is noteworthy that laser powers beyond 0.6 mJ mm^{-2} led to a decrease in the ON/OFF intensity changes, an effect attributed to secondary excitation of the photo-induced excited state possibly creating on a non-radiative relaxation pathway. To maximize the number of weak reflections observed, the pump–probe cycle for each frame was repeated three times before detector read-out. The pump–probe delay time was set at 100 ps. Much longer delay times caused spot extension in the ON frames, as observed in earlier experiments (Coppens, Benedict *et al.*, 2010). Laser-OFF and Laser-ON frames were collected in immediate succession to minimize the effect of long-range fluctuations in the beam parameters. The OFF/ON pump–probe cycle was repeated ten times for each frame to allow subsequent statistical filtering of the data. This redundancy is made possible by the extremely fast data collection, limited essentially by the ~ 4 s read-out time used with the MAR detector. Six sufficiently large data sets covering at least half of the reciprocal space within the resolution limit, totaling three each

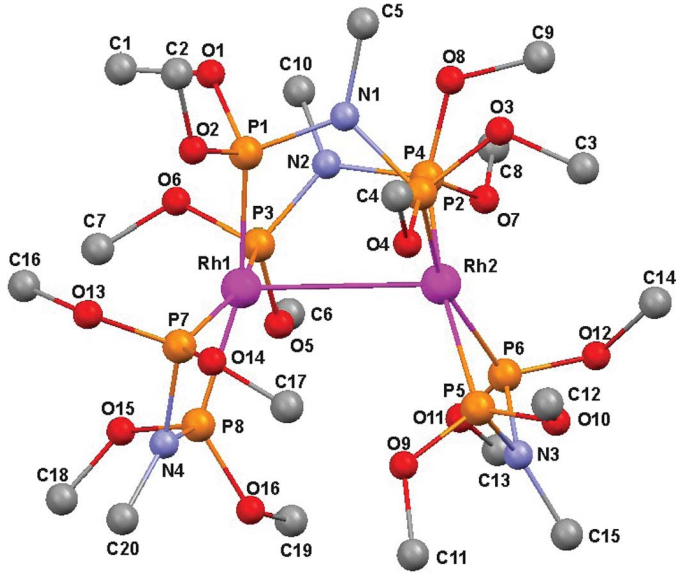

Figure 1
Molecular diagram of (1) and labeling of atoms.

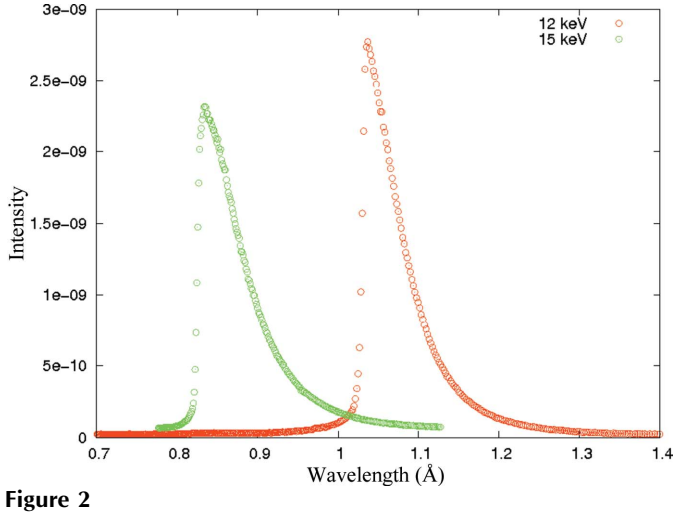

Figure 2
Experimental spectral distribution at BIOCARS beamline 14-ID prior to the experiments.

[1] Crystallographic information on the ground-state structure discussed in this paper is available from the IUCr electronic archives (Reference: SH5129). Services for accessing these data are described at the back of the journal.

at 12 and 15 keV, were collected each at successive values of the φ angle of the diffractometer with $\Delta\varphi = 5^\circ$ and were used in the subsequent analysis. Other runs had to be aborted because of premature laser damage of the samples as evident from pronounced weakening of the diffraction pattern and smearing of the diffraction spots. Details of the six data sets are summarized in Table 2 and Table S1 of the supplementary material.

The mutual consistence of the data sets was examined by the construction of correlation plots (Coppens *et al.*, 2005), two of which are shown in Fig. 4.

Table 2
Description of the data sets.

The last three columns are defined in equations (1)–(4)

Data set	No. of reflections after merging	Undulator setting (keV)	Sample size (μm)	Laser power (mJ mm^{-2})	$\langle\lvert\eta\rvert\rangle$	$k(\eta)$	k_B from Wilson plots
19	1196	12	$\sim 30 \times 20 \times 20$	0.60	0.056	1.061	1.112
20	588	12	$30 \times 20 \times 10$	0.60	0.089	0.667	1.258
24	540	12	$30 \times 40 \times 10$	0.55	0.096	0.619	1.310
27	760	15	$42 \times 22 \times 8$	0.45	0.060	0.990	1.081
28	1281	15	$43 \times 27 \times 12$	0.45	0.048	1.238	1.068
29	1150	15	$37 \times 32 \times 12$	0.45	0.043	1.381	1.065

2.3. Data processing

The reflections were indexed using the program *PRECOGNITION* (Ren, 2010), as well as using a new program *LAUEUTIL* currently being developed in our laboratory (to be published). Spot integration was performed by the program *LAUEGUI* (Messerschmidt & Tschentscher, 2008; Peters, 2003). The program is based on the seed–skewness method (Bolotovsky & Coppens, 1997), which does not require profile fitting. Only reflections with $I > 10\sigma(I)$, where $\sigma(I)$ is the statistical standard deviation of the measured intensity I, were considered in the calculation of the ON/OFF ratios R and related response ratios η, respectively defined as

$$R(hkl) = I_{\rm ON}/I_{\rm OFF} \qquad (1a)$$

and

$$\eta(hkl) = \frac{I_{\rm ON}(hkl) - I_{\rm OFF}(hkl)}{I_{\rm OFF}(hkl)} = R(hkl) - 1. \qquad (1b)$$

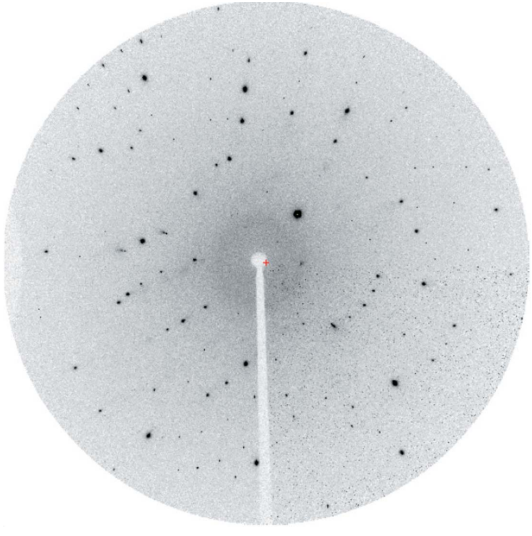

Figure 3
Single-pulse Laue image collected at the APS ID-14, BIOCARS beamline.

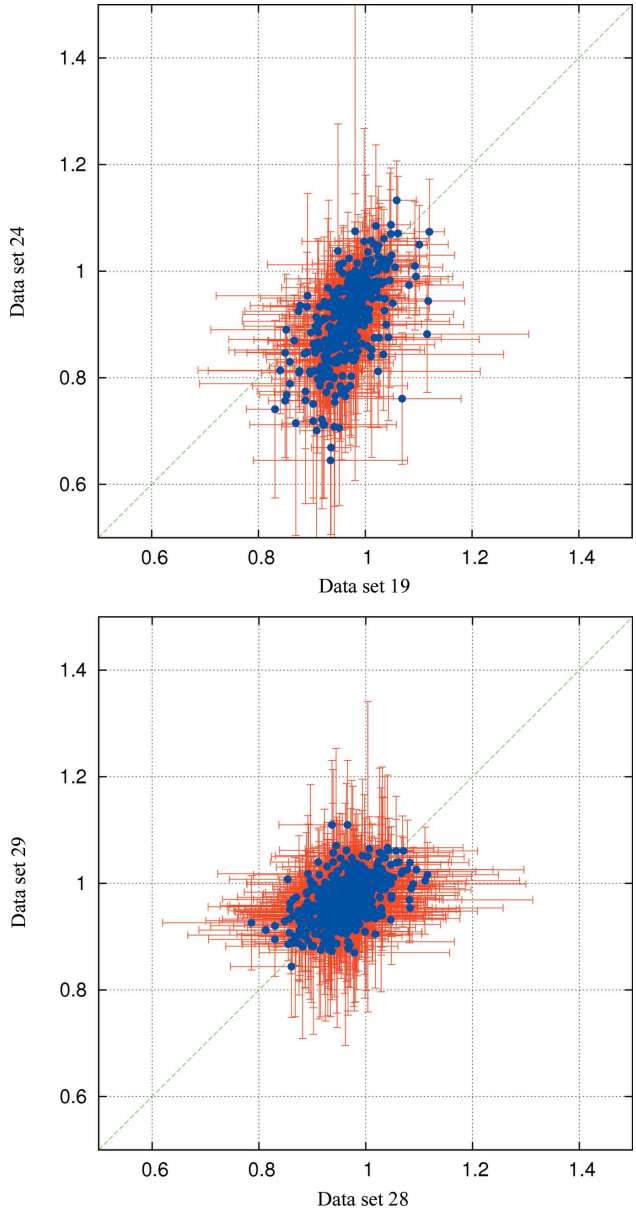

Figure 4
Examples of plots showing the correlation between ON/OFF ratios of individual *hkl*s in different data sets. Red lines correspond to $\pm 1\sigma(R)$. The green line represents a trend line for an ideal correlation ($y = x$). The data in the upper figure do not follow this trend, indicating a stronger overall response of data set 24.

Several filtering steps were applied. For each *hkl* on a frame the ten repeated ratio measurements were rejected whenever the standard deviation for the sample was larger than 0.5. Reflections with less than ten repeated measurements were also rejected. The resulting ratios were averaged over repeated and symmetry-equivalent measurements with the program *SORTAV* (Blessing, 1997). Outliers were down-weighted by the use of the robust/resistant Tukey biweighting criterion based on the deviation of individual measurements from the median (Blessing, 1997). Details are given in Table S2. The ten individual intensities of two reflections with $I_{ON} > I_{OFF}$ are shown in Fig. S1.

2.4. Preliminary scaling of the data sets collected on different crystals

To obtain a photodifference map for visualization of the light-induced changes and for extraction of initial atomic positions for the excited-state least-squares refinement, it is necessary to combine the data sets, as reliable Fourier maps essentially require a complete set of terms in the Fourier summation. In the RATIO method the ON data are obtained by multiplication of the monochromatic intensities by the synchrotron-determined ratios *R*,

$$I_{ON}(hkl) = I_{monochromatic}(hkl)R(hkl). \quad (2)$$

For multi-sample data sets with different fractional excitation the ratios must be reduced to a common scale before the Fourier summation is performed. To accomplish this the η values of individual reflections are scaled in *SORTAV* (Blessing, 1997) by $\langle|\eta|\rangle_{set}/\langle|\eta|\rangle_{all}$, in which $\langle|\eta|\rangle_{all}$ and $\langle|\eta|\rangle_{set}$ are the averages over all measured reflections and over the reflections in the specific set respectively. Corrected values of *R* are obtained from

$$k(\eta)_{set} = \langle|\eta|\rangle_{all}/\langle|\eta|\rangle_{set} \quad (3a)$$

$$\eta_{scaled}(hkl) = \eta(hkl)k(\eta)_{set} \quad (3b)$$

$$R_{scaled}(hkl) = 1 + \eta_{scaled}(hkl). \quad (3c)$$

The scaled and merged ratios are then used in equation (2) to generate uniform I_{ON} values for the calculation of photo-difference maps.

2.5. Analysis of the sample temperature during the ON measurements

An estimate of the temperature increase caused by the laser pulse can be obtained from a photo-Wilson plot (Schmøkel *et al.*, 2010; Vorontsov & Coppens, 2005). The plot gives an estimate of ΔB, which with the value of $\langle B\rangle$ from the monochromatic data measured at the same temperature can be converted to a temperature scale factor representing the relative temperature increase with the equation

$$k_B = \frac{B + \Delta B}{B} = 1 + \frac{\Delta B}{B}. \quad (4)$$

As may be expected, the values of k_B for each set are correlated with $\langle|\eta|\rangle_{set}$ as shown in Fig. 5. However, they become almost equal after the scaling according to equations (3*c*) and (2) is implemented.

The value of k_B for the set of combined data equals 1.07.

2.6. Least-squares refinement

The data were refined with the program *LASER*, which is based on the refinement of the response ratios (Vorontsov *et al.*, 2010). The program assumes a random spatial distribution of the excited-state species with a scattering formalism

$$F_{ON}(hkl) = (1 - P)F_{ON,GS}(hkl) + PF_{ON,ES}(hkl) \quad (5a)$$

and

$$F_{OFF}(hkl) = F_{OFF,GS}(hkl) \quad (5b)$$

in which F_{ON} and F_{OFF} are the structure factors for the light-ON and light-OFF measurements, GS and ES are the ground and excited state, respectively, and *P* is the percentage conversion to the light-induced state. An alternative algorithm assuming clustering of the light-induced species leads to quite different calculated values of the ON structure factors and has not been successful in any of our previous studies (Vorontsov

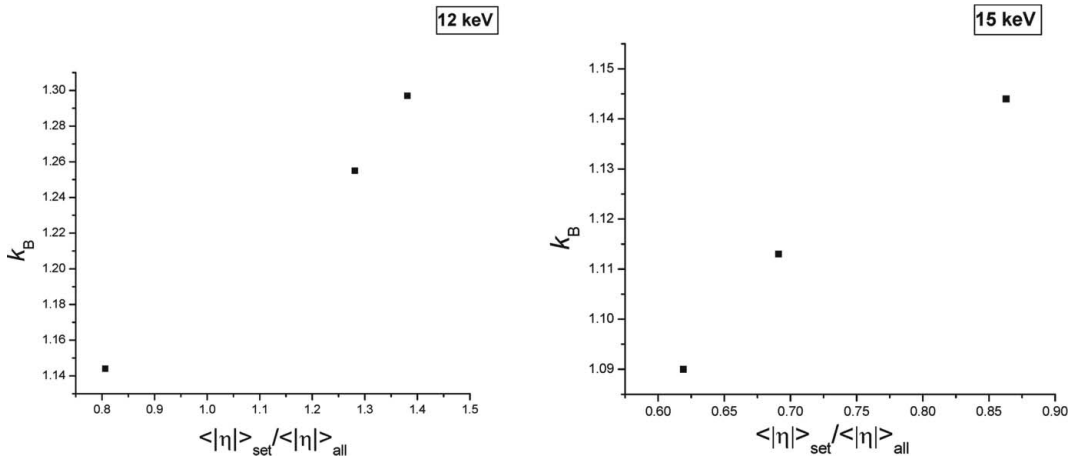

Figure 5
Relation between the temperature scale factor k_B and $1/k(\eta)$, the inverse of the response ratio scale factor for the 12 and the 15 keV data sets.

& Coppens, 2005). Differences between $F_{ON,GS}(hkl)$ and $F_{OFF,GS}(hkl)$, which would imply a motion or deformation of the GS molecules in the light-exposed crystal are expected to be minimal in this work because of the low conversion percentages achieved (Table S3). The *LASER* program allows for the refinement of up to six different data sets with individual values of the conversion percentage P and the temperature scale factor k_B and calculates R factors specifically designed for photocrystallographic experiments (Vorontsov *et al.*, 2010; Coppens, Kamiński & Schmøkel, 2010).

Refinement was performed on the six data sets listed in Table 2. Only data with $|\eta|/\sigma(\eta) > 1$ were used in the refinement giving a total of 2256 independent reflections for the refinement of 42 excited-state structure parameters. They included the six positional parameters of the two Rh atoms, temperature scale factors k_B, and the excited-state occupancies for each of six experimental runs plus three rotational and translational parameters of the four rigid PNP groups. The ground-state Rh positions were taken as starting points in the excited-state refinement of the Rh atoms. The ligands pivoted around anchor atoms, the positions of which were allowed to translate. For the two terminal ligands the initial positions of the anchor atoms were the locations of the excited-state Rh atoms to which the ligands were attached, obtained in a preliminary refinement of the Rh positions only. For the bridging ligands the midpoint of the Rh atoms was used as the starting position in the subsequent refinement. Structural results are presented in Tables 3 and 4 and S2–S4. Final agreement factors, defined elsewhere (Coppens, Kamiński & Schmøkel, 2010), are $R(\eta)$ = 0.342 and $R(R)$ = 0.034. Further numerical details on the refinement are given in Tables S5–S7.

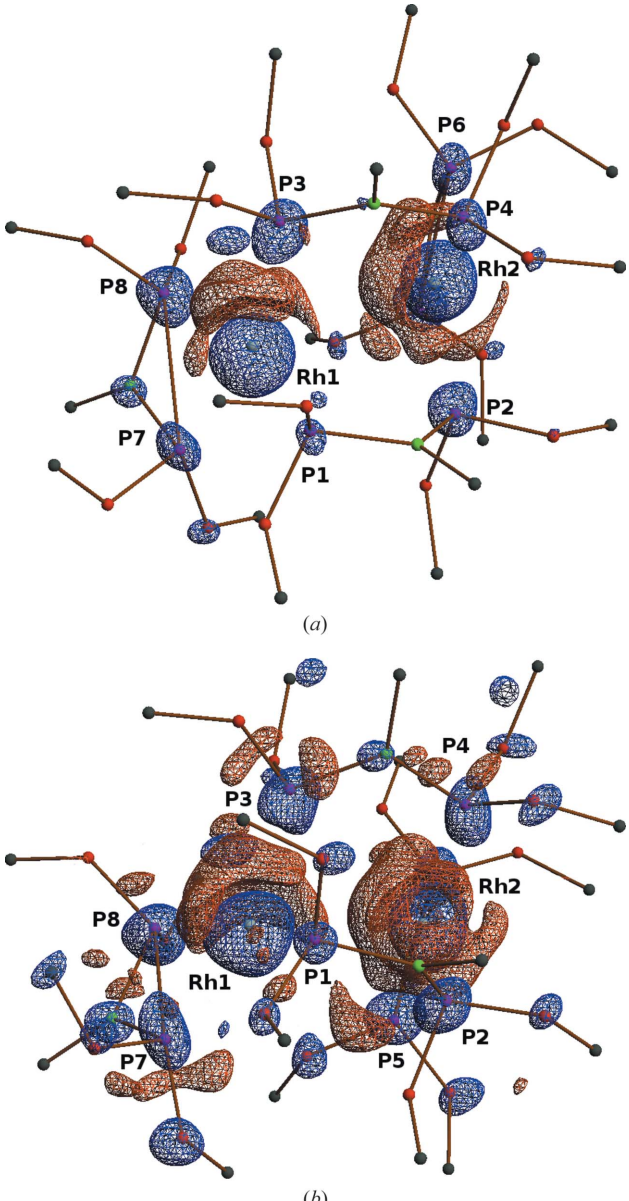

Figure 6
Photodifference maps with isosurfaces (red positive, blue negative) of ±0.25 e Å^{-3} (*a*) and ±0.175 e Å^{-3} (*b*) (calculated with *XDGRAPH* of the *XD* program set; Volkov *et al.*, 2006).

Table 3
Shifts of the Rh and P atoms on excitation and standard deviations (Å).

Atom	Shift	σ
Rh1	0.139	0.007
Rh2	0.134	0.005
P1	0.068	0.031
P2	0.099	0.035
P3	0.159	0.030
P4	0.112	0.029
P5	0.108	0.027
P6	0.067	0.027
P7	0.115	0.031
P8	0.105	0.026

3. Discussion of results

3.1. Photodifference maps

The photodifference map based on all independent reflections, calculated at isosurfaces of ± 0.25 e Å^{-3}, is shown in Fig. 6(*a*). The map indicates a sideward displacement of Rh1 and a displacement of Rh2 towards Rh1, thus suggesting both a rotation and a shortening of the Rh—Rh vector. In addition it shows a depletion of the electron density in the regions of P atoms. The compensating positive electron density at these atoms becomes visible when contours are drawn at the lower 0.175 e Å^{-3}. One of these maps is shown in Fig. 6(*b*).

3.2. The least-squares results

The results of the refinement on the excited-state Rh atom positions and the ligand translations and rotations are listed in Table 3. In agreement with the photodifference maps a significant change in the positions of the Rh atoms is observed. As Rh2 moves towards Rh1, but the latter is displaced in a perpendicular direction, the resulting bond shortening of 0.136 (8) Å (Table 4) is essentially a result of the Rh2 shift. The displacements of the P atoms are generally significant, but hardly affect the Rh—P distances, indicating that the ligands

Table 4
Experimental excited-state (ES) and ground-state (GS) bond lengths and their differences (Å).

		ES geometry		GS geometry			
Atom 1	Atom 2	Distance	σ	Distance	σ	Difference	Nature of ligand
Rh1	Rh2	3.045	0.008	3.1805	0.0002	**−0.136**	
Rh1	P1	2.269	0.033	2.2512	0.0006	0.018	Bridging
Rh2	P2	2.236	0.028	2.2631	0.0006	−0.027	
Rh1	P3	2.256	0.029	2.2736	0.0006	−0.018	Bridging
Rh2	P4	2.249	0.030	2.2552	0.0006	−0.006	
Rh2	P5	2.314	0.028	2.2796	0.0006	0.035	Terminal
Rh2	P6	2.280	0.030	2.2606	0.0006	0.020	
Rh1	P7	2.322	0.022	2.2769	0.0006	0.045	Terminal
Rh1	P8	2.217	0.022	2.2746	0.0006	−0.058	

Table 5
Isolated-molecule theoretical bond lengths obtained with *GAUSSIAN09* B3LYP functional (Å).

Basis set	GS	ES	Δ
LANL2DZ	3.670	3.031	0.639
6-31G*	3.620	3.138	0.482
6-311G*	3.667	3.115	0.552
WTBS for Rh+ 6-311G*	3.774	3.268	0.506

Table 6
Isolated-molecule theoretical bond lengths obtained with the BP86 functional.

DZ: double zeta, DZP: double zeta+ polarization functions, QZ4P: coreTZ, Valence 4Z + 4 polarization functions.

Basis set	GS	ES	Δ
Gaussian			
LANL	3.364	2.941	0.423
6-31G*	3.386	3.057	0.329
6-311G*	3.439	3.069	0.370
WTBS for Rh+6-311G*	3.650	3.186	0.464
ADF			
TZP	3.453	3.079	0.374
QZ4P	3.403	–	–

Table 7
Theoretical results (BP86 functional, *ADF* program) for (1) confined in a crystal cavity as calculated with the QM/MM method (Å).

Basis set	GS	ES	Δ	Experimental Δ
DZ	3.209	2.995	−0.214	−0.136 (8)
TZP	3.336	3.179	−0.157	

follow the metal atoms. The rigid-body rotations do not exceed 2.5°, but are more pronounced for the terminal ligand attached to Rh1 than for that linked to Rh2 as may be expected from the shift perpendicular to the Rh—Rh bond of the former atom.

A diagram of the molecule illustrating the atomic displacements on excitation is shown in Fig. 7.

3.3. Comparison with theory

Theoretical DFT calculations were performed both with *GAUSSIAN09* (Frisch *et al.*, 2009) and with the *Amsterdam Density Functional* program (Velde *et al.*, 2001). Two different functionals BP86 and B3LYP were used with a number of different basis functions. It is noticeable that even the isolated molecule Rh—Rh distance, determined as 3.183 Å, is calculated considerably longer by all theoretical isolated molecule treatments as shown in Tables 5 and 6. The results are slightly better with the BP86 functional applied with both programs (Table 6), but the bond length and its shortening of 0.136 (8) Å on transition to the triplet state are not well reproduced with either functional, independent of the basis set used. The large discrepancies are at least in part attributed to the effect of the crystal environment on the geometry of both the ground and excited states.

In an earlier study we applied the mixed quantum-mechanical (QM)/molecular-mechanics (MM) technique to explore the effect of the crystalline environment on the molecular dimensions. In our application the crystal environment is kept constant at the experimental values, while the complex in the crystalline cavity is optimized subject to the constraint imposed by the neighboring atoms (Kaminski *et al.*, 2010). Results of the QM/MM optimization for the cation of (1) performed with the *ADF* program using the BP86 functional with different basis sets are tabulated in Table 7.

The results confirm that the molecule in the crystal is severely constrained by its crystalline environment, even in the ground state. The ground-state Rh—Rh bond length is best approximated by the smaller basis set DZ (double zeta) calculation, but this result is likely to be fortuitous as the HOMO and LUMO diagrams obtained with this basis set significantly deviate from those from the more advanced calculations. The contraction calculated with the larger TZP

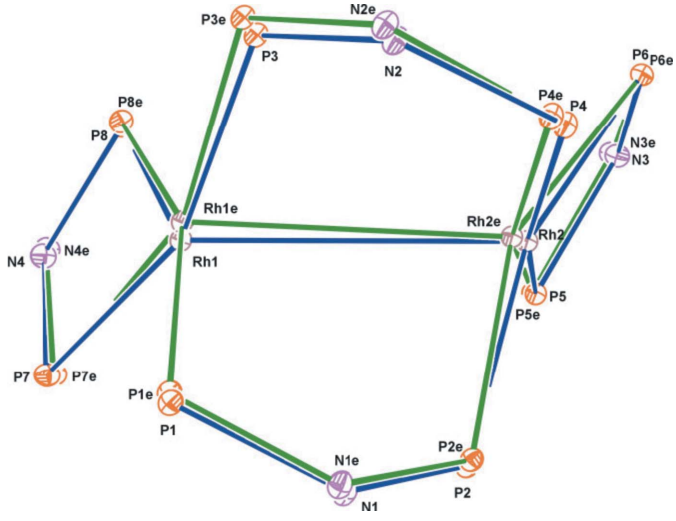

Figure 7
Molecular diagram indicating atomic shifts on laser excitation. Blue lines: ground state; green lines: excited state. The excited-state atoms are marked with 'e' after the label. Ellipsoids are drawn at the 5% probability level for the sake of clarity.

basis is within three standard deviations from the experimental result. The HOMO and LUMO orbital diagrams shown in Fig. 8 indicate an antibonding-to-bonding transition. They are remarkably similar to the diagrams observed in the time-resolved study of the $[Rh^{II}_2(1,8\text{-diisocyano-}p\text{-menthane})_4]^{2+}$ ion (2). However, in the latter case a much larger contraction of 0.85 (5) Å was observed in crystals of the PF_6^- salt. We note that the ground-state Rh—Rh bond length of (2) at 4.496 (1) Å is much longer than that of (1), leaving room for a much larger contraction.

Table 8
Calculated (QM/MM) and observed changes in the Rh—P distances Δ on excitation (Å).

QM/MM TZP	Ground	Excited	Δ(theory)	Δ(experimental)	σ(experimental)	
Rh1—P1	2.285	2.295	0.010	0.018	0.033	Bridging 1
Rh2—P2	2.297	2.276	−0.021	−0.027	0.028	
Rh1—P3	2.307	2.281	−0.026	−0.018	0.029	Bridging 2
Rh2—P4	2.281	2.284	0.003	−0.006	0.030	
Rh2—P5	2.324	2.320	−0.004	0.035	0.028	Terminal 1
Rh2—P6	2.311	2.339	0.028	0.020	0.030	
Rh1—P7	2.333	2.370	0.037	0.045	0.022	Terminal 2
Rh1—P8	2.330	2.338	0.008	−0.058	0.022	

The experimental changes in the Rh—P distance as determined by the rigid-body refinement of the PNP ligands are listed in Table 8. The changes are of the same magnitude as the standard deviations derived from those of the rotation and translation parameters of the refinement. Nevertheless, except for the Rh1—P8 distance there seems to be a clear correlation with the changes determined theoretically with the QM/MM method.

4. Conclusions

We conclude that the improved Laue method is capable of producing excited-state structures at atomic resolution of a quality at least comparable with those of monochromatic experiments. The much faster data collection allows the use of one of a few X-ray pulses per frame of data, and thus minimizes crystal damage caused by laser exposure of the samples. Equally important, the shorter exposure time optimizes the attainable time resolution. The experimental results are quantitatively supported by the QM/MM calculations which take into account the confining effect of the crystal environment, but not by theoretical results on the isolated complex. This effect has to be taken into account in the interpretation of photochemical properties of molecules in the solid state.

We would like to thank Robert Henning and Tim Graber of BioCARS for assistance and advice with the data collection. This work was funded by the Division of Chemical Sciences, Geosciences, and Biosciences, Office of Basic Energy Sciences of the US Department of Energy, through grant DEFG02-ER15372. Use of the BioCARS Sector 14 was supported by the National Institutes of Health, National Center for Research Resources, under grant number RR007707. The time-resolved facility at Sector 14 was funded in part through a collaboration with Philip Anfinrud (NIH/NIDDK). The Advanced Photon Source is supported by the US Department of Energy, Office of Basic Energy Sciences, under Contract No. W-31-109-ENG-38.

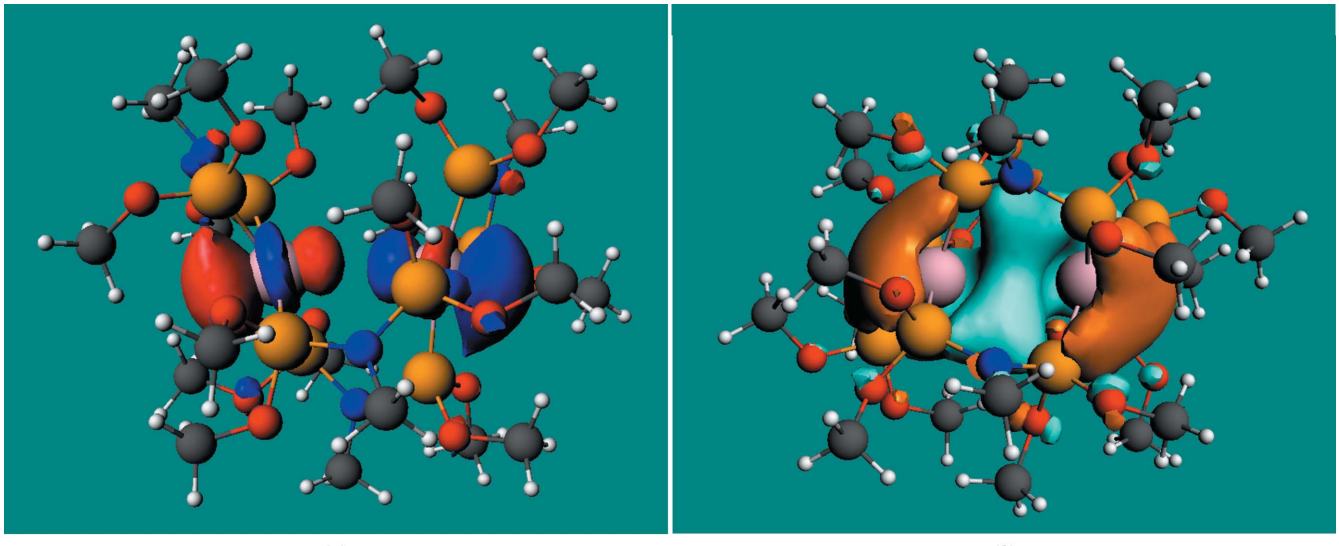

(*a*) (*b*)

Figure 8
The HOMO (*a*) and the LUMO (*b*) of the title complex (TZP basis, BP86 functional, QM/MM results, isolated-molecule orbitals are essentially identical). Isovalue surfaces at ±0.0275 a.u. Blue/blue–grey positive, red/orange negative.

References

Benedict, J. B., Makal, A., Sokolow, J. D., Trzop, E., Scheins, S., Henning, R., Graber, T. & Coppens, P. (2011). *Chem. Commun.* **47**, 1704–1706.

Blakley, R. L., Yin, Y., Lloyd, C., Mague, J. T. & McPherson, G. L. (1989). *Chem. Phys. Lett.* **157**, 398–402.

Blessing, R. H. (1997). *J. Appl. Cryst.* **30**, 421–426.

Bolotovsky, R. & Coppens, P. (1997). *J. Appl. Cryst.* **30**, 244–253.

Cailleau, H., Lorenc, M., Guérin, L., Servol, M., Collet, E. & Buron-Le Cointe, M. (2010). *Acta Cryst.* A**66**, 189–197.

Coppens, P., Benedict, J., Messerschmidt, M., Novozhilova, I., Graber, T., Chen, Y.-S., Vorontsov, I., Scheins, S. & Zheng, S.-L. (2010). *Acta Cryst.* A**66**, 179–188.

Coppens, P., Kamiński, R. & Schmøkel, M. S. (2010). *Acta Cryst.* A**66**, 626–628.

Coppens, P., Pitak, M., Gembicky, M., Messerschmidt, M., Scheins, S., Benedict, J., Adachi, S., Sato, T., Nozawa, S., Ichiyanagi, K., Chollet, M. & Koshihara, S. (2009). *J. Synchrotron Rad.* **16**, 226–230.

Coppens, P., Vorontsov, I. I., Graber, T., Gembicky, M. & Kovalevsky, A. Y. (2005). *Acta Cryst.* A**61**, 162–172.

Frisch, M. J. *et al.* (2009). *GAUSSIAN*09, Revision A.1. Gaussian Inc., Pittsburgh, Pennsylvania, USA.

Kaminski, R., Schmøkel, M. S. & Coppens, P. (2010). *J. Phys. Chem. Lett.* **1**, 2349–2353.

Mague, J. T. (1995). *Inorg. Chim. Acta*, **229**, 17–25.

Messerschmidt, M. & Tschentscher, T. (2008). *Acta Cryst.* A**64**, C611.

Peters, J. (2003). *J. Appl. Cryst.* **36**, 1475–1479.

Ren, Z. (2010). *Precognition User Guide*. RenZ Research, Inc, Illinois, USA.

Schmøkel, M. S., Kamiński, R., Benedict, J. B. & Coppens, P. (2010). *Acta Cryst.* A**66**, 632–636.

Velde, G. T., Bickelhaupt, F. M., Baerends, E. J., Guerra, C. F., Gisbergen, S. J. A. V., Snijders, J. G. & Ziegler, T. (2001). *J. Comput. Chem.* **22**, 931–967.

Volkov, A., Macchi, P., Farrugia, L. J., Gatti, C., Mallinson, P. R., Richter, T. & Koritsanszky, T. (2006). *XD*2006. Middle Tennessee State University, USA, Università di Milano and CNR-ISTM Milano, Italy, University of Glasgow, Scotland, State University of New York at Buffalo, USA, and Freie Universität Berlin, Germany.

Vorontsov, I. I. & Coppens, P. (2005). *J. Synchrotron Rad.* **12**, 488–493.

Vorontsov, I., Pillet, S., Kamiński, R., Schmøkel, M. S. & Coppens, P. (2010). *J. Appl. Cryst.* **43**, 1129–1130.